Evaluation of experimental, analytical, and computational methods to determine long-bone bending stiffness

Caitlyn J. Collins, Baixuan Yang, Thomas D. Crenshaw, Heidi-Lynn Ploeg

PII: S1751-6161(20)30791-8

DOI: https://doi.org/10.1016/j.jmbbm.2020.104253

Reference: JMBBM 104253

To appear in: *Journal of the Mechanical Behavior of Biomedical Materials*

Received Date: 15 August 2020

Revised Date: 8 November 2020

Accepted Date: 6 December 2020

Please cite this article as: Collins, C.J., Yang, B., Crenshaw, T.D., Ploeg, H.-L., Evaluation of experimental, analytical, and computational methods to determine long-bone bending stiffness, *Journal of the Mechanical Behavior of Biomedical Materials* (2021), doi: https://doi.org/10.1016/j.jmbbm.2020.104253.

Author Statement:

Caitlyn Collins: Conceptualization, Methodology, Investigation, Software, Formal Analysis, Data Curation, Writing - Original Draft, Writing – Reviewing and Editing

Baizuan Yang: Investigation, Software, Formal Analysis, Data Curation

Thomas Crenshaw: Resources, Writing – Reviewing and Editing

Heidi-Lynn Ploeg: Conceptualization, Supervision, Data Curation, Writing – Reviewing and Editing

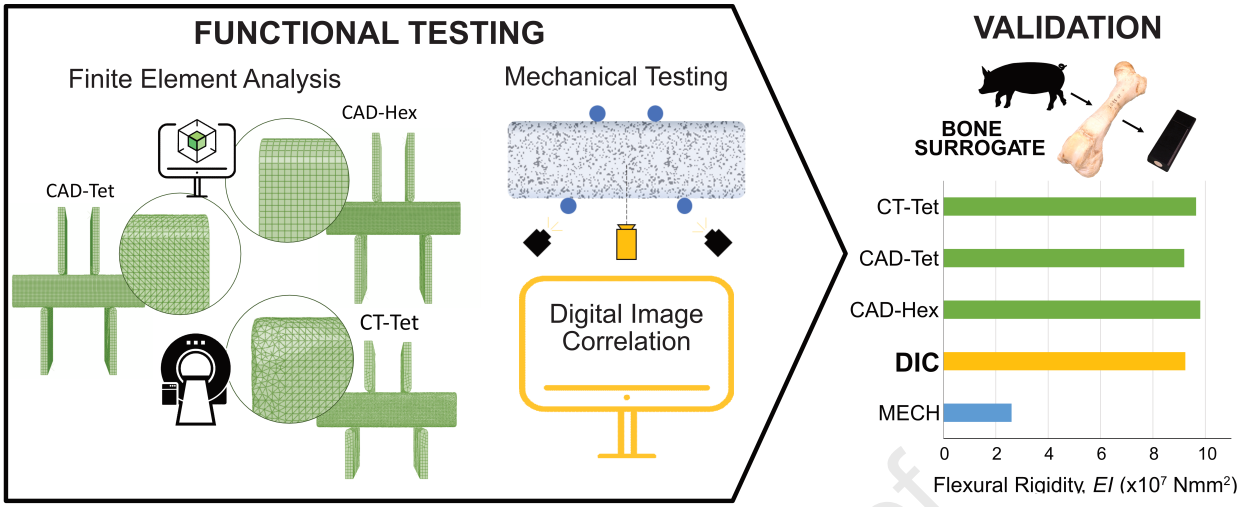

Evaluation of Experimental, Analytical, and Computational Methods to Determine Long-Bone Bending Stiffness

Caitlyn J. Collins[a,b,1], Baixuan Yang[a,c], Thomas D. Crenshaw[d], Heidi-Lynn Ploeg[a,c]

[a]Department of Mechanical Engineering, University of Wisconsin-Madison, Madison, WI, United States of America
[b]Department of Health Sciences and Technology, Institute for Biomechanics, ETH Zurich, Zurich, Switzerland
[c]Department of Mechanical and Materials Engineering, Queen's University, Kingston, ON, Canada
[d]Department of Animal and Dairy Sciences, University of Wisconsin-Madison, Madison, WI, United States of America

Corresponding Author:
[1]Caitlyn J. Collins
caitlyn.collins@hest.ethz.ch
Leopold-Ruzicka-Weg 4, HCP H 11.3
8093 Zurich, Switzerland
+41 44 633 9199

Declarations of interest: none

ABSTRACT

Methods used to evaluate bone mechanical properties vary widely depending on the motivation and environment of individual researchers, clinicians, and industries. Further, the innate complexity of bone makes validation of each method difficult. Thus, the purpose of the present research was to quantify methodological error of the most common methods used to predict long-bone bending stiffness, more specifically, flexural rigidity (EI). Functional testing of a bi-material porcine bone surrogate, developed in a previous study, was conducted under four-point bending test conditions. The bone surrogate was imaged using computed tomography (CT) with an isotropic voxel resolution of 0.625 mm. Digital image correlation (DIC) of the bone surrogate was used to quantify the methodological error between experimental, analytical, and computational methods used to calculate EI. These methods include the application of Euler Bernoulli beam theory to mechanical testing and DIC data; the product of the bone surrogate composite bending modulus and second area moment of inertia; and finite element analysis (FEA) using computer-aided design (CAD) and CT-based geometric models. The methodological errors of each method were then compared. The results of this study determined that CAD-based FEA was the most accurate determinant of bone EI, with less than five percent difference in EI to that of the DIC and consistent reproducibility of the measured displacements for each load increment. CT-based FEA was most accurate for axial strains. Analytical calculations overestimated EI and mechanical testing was the least accurate, grossly underestimating flexural rigidity of long-bones.

KEYWORDS: bone bending stiffness, digital image correlation, finite element analysis, validation

HIGHLIGHTS

- Flexural rigidity (EI) of long bones is commonly used to assess treatment effects
- Digital image correlation measurements on bone surrogate quantified accurate EI
- Bending tests of bone surrogate underestimated EI by 72%
- Euler-Bernoulli beam theory overestimated EI by 45%
- EI from CAD- and CT-based finite element analyses are accurate to within 6%

1 INTRODUCTION

Musculoskeletal conditions are the highest contributor to global disabilities and affect 20-33% of the population(James et al., 2018). Approximately 54% of adults over the age of 50 in the United States suffer from osteoporosis, a degenerative bone disease associated with increased risk of bone fracture(Wright et al., 2014). The annual incidence of osteoporotic related fracture is projected to exceed three million by 2025 (Burge et al., 2007). During the first three months after an osteoporotic related hip fracture, women and men are at a six- and eight-times greater risk of morbidity, respectively. Even at ten years post fracture, patients who suffer osteoporotic related hip fracture remain at a two times greater risk of mortality than the general population (Bliuc et al., 2009). The scale and breadth of musculoskeletal conditions motivates a range of research studies into prevention and treatment methods.

Preventative treatments for osteoporotic fracture include antiresorptives and anabolic therapies. However, both have limited efficacy, adverse side effects, and the optimal dosage and duration of use is still unknown (Iolascon et al., 2020; McClung et al., 2014; Ruggiero et al., 2004; Wysowski and Greene, 2013). Early detection of a loss in bone mechanical properties is necessary since preventative treatment options are limited and the consequences of osteoporotic fracture are so high. Elastic modulus and

second moment of area are key parameters for fracture risk assessment. Both fracture toughness and flexural rigidity rely on accurate estimates of structural and material stiffness. For example, osteoporosis has been shown to increase material stiffness but decrease fracture toughness (Morais et al., 2010). Image-based finite element analysis (FEA) is another method to predict fracture, as demonstrated by Kluess and co-workers (Kluess et al., 2019). For this to be effective, accurate structural and material properties are required. Also, inverse methods which capitalize on image-based FEA have been used to account for subject specific differences in the conversion of computed tomography (CT) density to elastic modulus (Rezaei et al., 2019). Subject specific parameters such as age and sex, both of which affect the pathophysiology of osteoporosis, can then be incorporated in fracture prediction methods (Dy et al., 2011).

In vitro mechanical testing is the most common determinant of bone stiffness but is limited to destructive methods. Dual-energy x-ray absorptiometry (DXA) is the standard clinical method for determining changes in apparent bone density, a contributing factor to bone stiffness. DXA, however, is a poor evaluator of bone mechanical properties as it only yields a measure of areal bone mineral density and does not provide three-dimensional (3D) density information. In contrast, specimen or patient-specific 3D geometry and material properties are captured with CT image-based analytical and finite element methods(Leslie and Morin, 2020). The accuracy of bone stiffness calculations is dependent on meeting the assumptions of the underlying equations from classical mechanics(Arias-Moreno et al., 2020; Schriefer et al., 2005; Sommers et al., 2007; van Lenthe et al., 2008). Image-based FEA is arguably the most accurate of the

methods used to determine bone stiffness (Leslie and Morin, 2020); however, image-based FEA requires validation and is computationally expensive.

Although all methods detailed above can be used to quantify bone stiffness, the innate complexity of bone makes validation of each method difficult. Therefore, a bi-material and CT scan compatible surrogate was developed (Collins et al., 2018) to provide consistent reproducible mechanical properties for methodological evaluation of experimental, analytical, and computational bone bending stiffness. In the current study, the errors in bone bending stiffness derived from Euler-Bernoulli beam bending theory, FEA, and crosshead deflection during mechanical testing are quantified against experimental measurements with digital image correlation (DIC).

2 MATERIALS AND METHODS

2.1 Four-point bending

A fabricated, bi-material and CT scan compatible bone surrogate with a locational translational fit (N7/h6) between the core (high-density polyurethane (HDPU)) and shell (acetyl copolymer (AC)) was selected for functional testing. Development and design of the surrogate is detailed in a previous study (Collins et al., 2018). The surrogate underwent repeat four-point bending tests (n=3) using an MTS Sintech 10/GL testing machine (MTS, Eden Prairie, MN) with displacement rate of 5.0 mm/min. The distances between upper and lower supports were 12.7 mm (a) and 50.8 mm (L), respectively. Support diameter, D, was 5 mm. The surrogate was loaded within the linear-elastic region of the surrogate, well below the yield point. Force and displacement data were directly measured from the MTS testing system load cell and crosshead,

respectively. The Hertzian contact (Puttock et al., 1969) equation (Eq. (1)) for a cylinder on a plane was used to determine the theoretical local deformation, *y*, of the surrogate at the point of contact with the supports. Here, $\bar{F}$ is the applied force per unit length of contact (i.e. width of the surrogate, *w* = 37.5 mm), and v_1, v_2, E_1, and E_2 are the Poisson's ratios and elastic moduli of the steel support and AC shell, respectively, as described in detail (Collins et al., 2018). Effective flexural rigidity (EI_{eff}) of the surrogate was calculated at the peak load increment using Euler-Bernoulli (EB) beam theory for prismatic, long beams in pure bending (Eq. (2) (Young et al., 2002)). Here, K_s is the bending stiffness of the surrogate, calculated from the peak force, *F*, and the peak deflection, *δ,* corrected for Hertz contact (Eq. (3)), and *x* (12.7 mm) is the position of the measured displacement.

$$y = \bar{F}\left(\frac{1-{v_1}^2}{\pi E_1}+\frac{1-{v_2}^2}{\pi E_2}\right)\left[1+ln\left\{\frac{8\left(\frac{w}{2}\right)^2}{\left(\frac{1-{v_1}^2}{\pi E_1}+\frac{1-{v_2}^2}{\pi E_2}\right)\bar{F}D}\right\}\right] \quad (1)$$

$$EI = \frac{a\left(3Lx-3x^2-a^2\right)K_s}{12} \quad (2)$$

$$K_s = \frac{F}{\delta-2y} \quad (3)$$

2.2 Digital Image Correlation

Following the initial tests, the surrogate was spray painted with a random black and white speckle pattern and subjected to additional repeat four-point bending tests (n=5) using the same MTS Sintech 10/GL testing machine (MTS, Eden Prairie, MN) and two-dimensional (2D) DIC equipment (Fig. 1). Four steps of incremental loads of approximately 1500 N, from 0 N to 6000 N, were applied to the surrogate and images were captured at each increment using a Grasshopper GRAS-50S5M camera with a 35 mm focal length lens (Point Grey Research, Richmond, BC, Canada). The camera was

positioned perpendicular to the surrogate at a distance of 35 cm. Contour plots of strain in the axial, x-direction ($\varepsilon_{xx,DIC}$) and displacement in the vertical, y-direction (δ_{DIC}), correlating to the approximate 1500 N load increments from 0 to 6000 N, were calculated using the Improved Digital Image Correlation Software (Eberl, 2010; Jones et al., 2014) in Matlab R2015a (MathWorks, Natick, Massachusetts). Each contour plot was sampled at positions perpendicular and parallel to the x-axis to track changes in $\varepsilon_{xx,DIC}$ and δ_{DIC} in response to load, respectively. The sampled $\varepsilon_{xx,DIC}$ and δ_{DIC} data were averaged at each load step for the repeat measurements and plotted with 95% confidence intervals (CIs) labelled for comparison to the results of other methods. DIC flexural rigidity (EI_{DIC}) of the surrogate was calculated for the ~6000 N load increment using Eq. (4) where F_{max} is the average maximum applied force (= 6026 N) and x (= 25.4 mm) is the position along the x-axis of the expected peak deflection (point B, Fig. 1). The total localised deflection of the surrogate at the points of contact with the supports (y_{DIC}) was approximated by averaging the calculated displacements at the x-position of the lower supports (points A and C, Fig. 1) in response to each load increment. For EI_{DIC}, δ was the peak deflection corrected for local displacement at the supports, calculated using the difference between δ_{DIC} at point B and y_{DIC} for the ~6000 N load step.

$$EI = \frac{-F_{max}(L-a)\left(\frac{L(x-a)^3}{L-a}-x^3+L^2-(L-a)^2x\right)}{12\delta L} + \frac{F_{max}a\left(\frac{L(x-L+a)^3}{a}-x^3+\left(L^2-a^2\right)x\right)}{12\delta L} \quad (4)$$

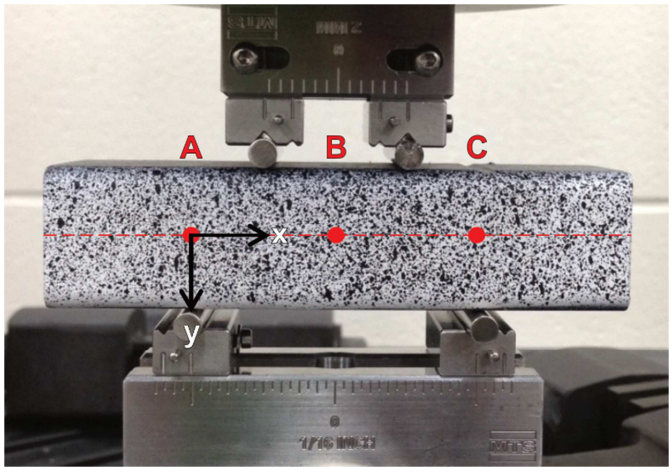

Fig. 1. Photo of the bone surrogate speckled for DIC between the four-point bending supports, with coordinate system and points A, B and C (x= 0, 25.4 mm, and 50. 8 mm) labelled.

2.3 Medical Imaging

The surrogate was CT scanned in air using a Discovery CT750 HD CT scanner (GE Healthcare, Little Chalfont, United Kingdom) with an isotropic voxel resolution of 0.625 mm (equal slice thickness and spacing) at 120 kV and 60 mA. CT images were reconstructed using accompanying scanner software with the GE “boneplus” algorithm and imported as Digital Imaging and Communications in Medicine (DICOM) images into the medical image processing software Mimics 17.0 (Materialise, Ann Arbor, MI). The surrogate was segmented into volume masks of the shell and core using thresholds of –139 to 640 and –678 to 244 HU for the AC and HDPU, respectively.

2.4 Finite Element Analysis

Finite element analyses (FEAs) were performed on CAD and CT-based models of the surrogate under four-point bending in Abaqus Explicit 2017 (Simulia, Providence, RI). The bone surrogate models were meshed using linear hexahedral elements with incompatible modes (C3D8R) or quadratic tetrahedral elements (TET10, C3D10) with a

maximum edge length of 1 mm (Fig. 2). Homogeneous, linear elastic material properties were assigned to the AC shell ($E_{b,AC}$ = 2850 MPa, v_{AC}=0.363 (Osswald and Menges, 2003)) and HDPU core ($E_{b,HDPU}$ = 596 MPa, and v_{HDPU}=0.3). Two load applicators were spaced 25.4 mm apart on the top surface of the bone surrogate. They were fixed in the z (perpendicular to bending plane) and x (principal beam axis) directions and moved vertically downward in the +y direction (Fig. 1) with a speed of 5 mm/minute. Two supports were positioned 50.8 mm apart at the bottom of the bone surrogate for which all degrees of freedom were fixed. The load applicators and supports were meshed using four-noded, three-dimensional, bilinear, rigid quadrilateral elements (R3D4) with a maximum edge length of 1 mm, shown in Fig. 2. A surface-to-surface contact algorithm was used between the bone surrogate models and the load applicators/supports with frictionless tangential behaviour and a “hard” contact pressure-overclosure relationship. A time period of 10 seconds was used for each load step and FEA results were written every 0.25 seconds.

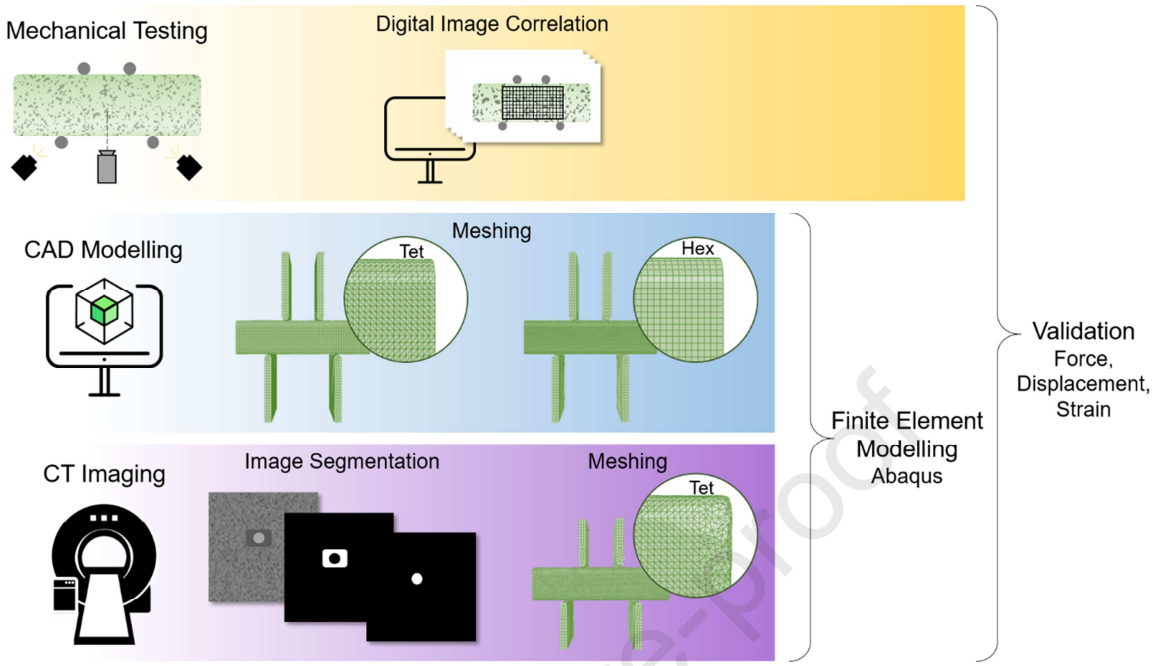

Fig. 2: Methods used to evaluate the flexural rigidity of the bone surrogate. Here the preprocessing steps and resultant meshes for CAD- vs CT-based finite element analysis are highlighted.

FEA displacement in the y-direction (δ_{FEA}) and FEA strain in the x-direction ($\varepsilon_{xx,FEA}$) were sampled along the face of the geometric models of the surrogate parallel and perpendicular to the x-axis (Fig. 1), respectively. δ_{FEA}, measured as the difference in displacement between points A and B in the y-direction (Fig. 1), and $\varepsilon_{xx,FEA}$ for the specified load intervals (0:1500:6000 N) were interpolated from the two closest FEA results in order to replicate the DIC test conditions. Effective flexural rigidity from the FEA data (EI_{FEA}) was calculated for the highest load increment using Eq. (4), where F was the total reaction force from the load applicators (6000N), δ was the δ_{FEA} at point B, and x (= 25.4 mm) was set to the x-position of point B (Fig 1).

2.5 Analytical Calculations

The analytical flexural rigidity (EI_x) was calculated in a previous study from the product of the composite second moment of area about the x-axis and the bending

modulus of the acetyl copolymer ($E_{b,AC}$) (Collins et al., 2018). Since the lower support span length to surrogate height ratio (roughly 2:1) is significantly smaller than recommended for negligible shear deformation (20:1), Eq. (5) was used to determine the appropriateness of using EB to evaluate the surrogate (Dolph, 1954; Gere and Timoshenko, 2000; Howe et al., 1951). This dimensionless number, *S*, provides a means to evaluate the importance of the shear rigidity, κAG, relative to that of the flexural rigidity (EI) and beam length. Here, κ is the calculated Timoshenko shear correction coefficient for rectangular cross sections (0.852) based on v_2, h is the height of the surrogate (25 mm), A is the total cross-sectional area of the surrogate (938 mm^2), and G is the shear modulus derived from $E_{b,AC}$ and v_2 (1050 MPa) (Eq. (5)). When S << 1, the Timoshenko beam theory for a uniform, static beam is equivalent to EB beam theory, indicating negligible shear deformation.

$$\boldsymbol{S = \frac{E_{b,AC}\left(\frac{wh^3}{12}\right)}{\kappa AGL^2}} \quad (5)$$

3 RESULTS AND DISCUSSION

A representative contour plot of δ_{DIC} at the peak load increment (6000 N) can be seen in Fig. 3. As expected, peak vertical deflections occurred between the upper supports, and contact deflections increased with increasing load: 0.06 mm, 0.12 mm, 0.18 mm, and 0.23 mm for 1500 N, 3000 N, 4500 N, and 6000 N, respectively.

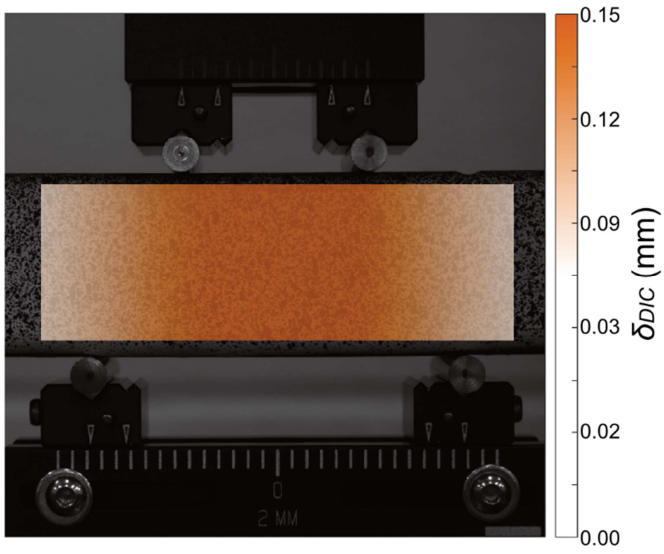

Fig. 3: Contour plot of the calculated DIC deflection (δ_{DIC}) at the peak load increment (6000N).

For comparison, the displacements from the DIC and FEA for all CAD-based and CT-based models were sampled along the horizontal midplane (i.e. at y=0 mm (Fig. 1)) at each 1500 N load increment and plotted (Fig. 5).

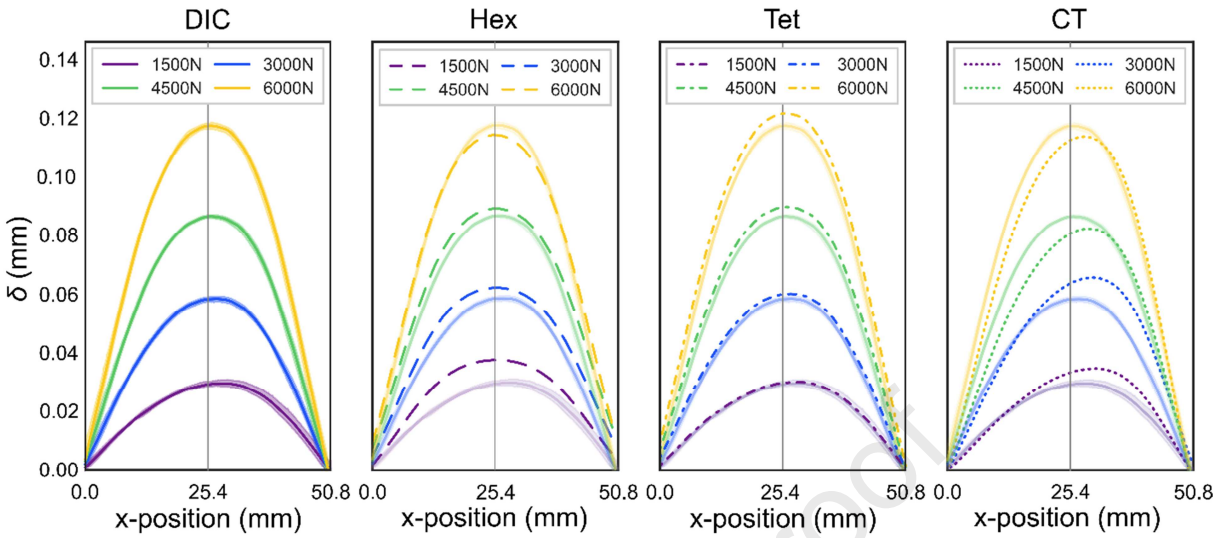

Fig. 4: Vertical deflection (δ) vs x-position for the 0, 1500, 3000, 4500, and 6000 N load increments, as measured by DIC (Left), CAD-based FEA with a Hex mesh (Left, Centre), CAD-based FEA with a Tet mesh (Right, Centre) and CT-based FEA with a Tet mesh (Right). δ_{DIC} data is presented as an average with 95% confidence intervals in each plot.

The repeatability of the DIC displacement measurements was relatively high, as evident by the relatively small CIs at each load increment. The largest variance was observed at the 1500 N load increment, where the ratio of displacement to spatial resolution is lowest. A slight skew was present in the DIC displacements, particularly at the lower load increments. This behaviour was closely matched for the CAD-based FEA with the Tet-mesh and somewhat mirrored in the CT-based FEA, while the CAD-based FEA with the Hex-mesh exhibited displacements that were symmetric about the bone surrogate/“beam” centre (point B, Fig. 1). Both the CT-based FEA and CAD-based FEA with the Hex-mesh over- and underestimated the DIC displacements, depending on the load increment, with the shift from over- to underestimation occurring at the 4500 N and 6000 N load increments, respectively. The deflections of the CAD-based FEA with the

Tet mesh nearly matched those of the DIC, with slight overestimations as the load increased (Fig. 4).

The accuracy of 2D DIC measurements is heavily dependent on the position of the camera relative to the observed object face. Any misalignment of the camera relative to the observed object face results in skewed displacement measurements. Although care was taken to ensure that the camera was level and perpendicular to the surface of the bone surrogate, post-processing of the DIC data revealed that the centre-to-centre distances for the cylindrical supports (as measured from the circular faces, both top and bottom sets) were slightly larger than the those of the test setup (ratio of 1.009). This indicates that the camera was positioned out of the x-y plane of the surrogate face (Fig. 3). This slight misalignment resulted in a measured displacement that was nearly 8% larger at x=34.1 mm than at x=19.4 mm when the applied load was 1500 N (Fig. 4). The relative effect of this camera misalignment decreased with increasing load and was less than 2% when the applied load was 6000 N.

A representative contour plot of the % $\varepsilon_{xx,DIC}$ at the peak load increment (6000 N) can be seen in Fig. 5. Strain values shifted from compressive to tensile from the top (y =-12.5 mm) to the bottom of the surrogate (y =12.5 mm), with peak strains occurring towards the centre of the surrogate (point B, Fig 1).

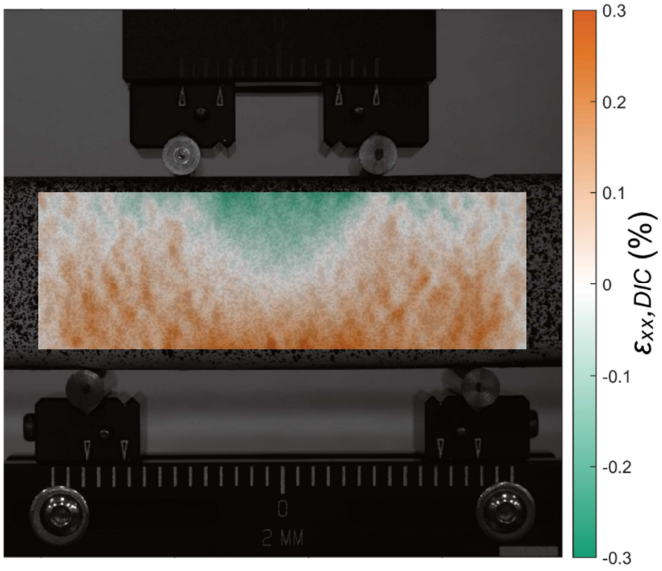

Fig. 5: Contour plot of the calculated DIC strain in the x-direction ($\varepsilon_{xx,DIC}$) at the peak load increment (6000N). Strain is reported as a percentage.

For comparison, the $\varepsilon_{xx,DIC}$ and $\varepsilon_{xx,FEA}$ for all CAD- and CT-based models were sampled along the vertical midplane (point B, Fig. 1) at each load increment and plotted in Fig. 6. The plane of zero strain occurred below the geometric neutral axis for both $\varepsilon_{xx,DIC}$ and $\varepsilon_{xx,FEA}$ for all models. Since the surrogate is a composite of AC and HDPU, which exhibit anisotropic material properties, the shift in the plane of zero strain towards the edge of the beam in tension may be a result of the more compliant tensile compared to compressive stiffness of both materials. However, the agreement between the DIC and FEA measurements infers that bulging of the material is not the sole cause of this shift in neutral axis. More than likely, the short and stout geometry of the beam resulted in combined loading due to shear forces at the points of contact between the beam and the supports, wherein the conditions of Saint-Venant's principle were not met.

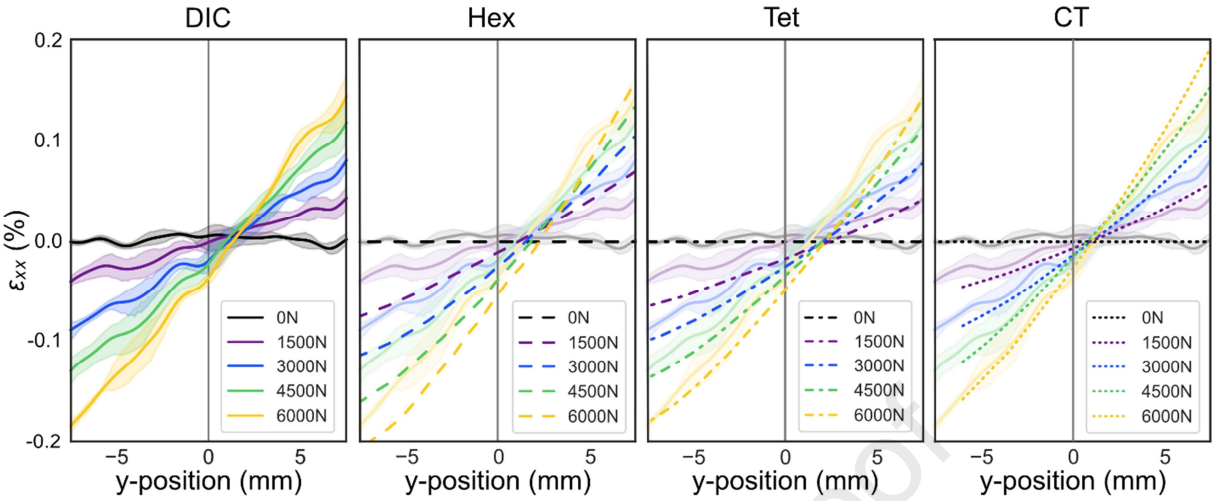

Fig. 6: Strain in the x-direction (ε_{xx}) versus y-position for the 0, 1500, 3000, 4500, and 6000 N load increments, as measured by DIC (Left), CAD-based FEA with a Hex mesh (Left, Centre), CAD-based FEA with a Tet mesh (Right, Centre) and CT-based FEA with a Tet mesh (Right). All strains are reported as a percentage and $\varepsilon_{xx,DIC}$ data are presented as an average with 95% confidence intervals in each plot.

In contrast to the displacement measurements, the variability of the DIC strain measurements was relatively high for all load increments. All three models overestimated $\varepsilon_{xx,DIC}$ on the compressive side of the beam, particularly at the 1500 N load increment. The CAD-based FEA with the Hex mesh performed the worst, with $\varepsilon_{xx,FEA}$ overestimating both compressive and tensile strains at each load increment. With increasing load, $\varepsilon_{xx,FEA}$ showed improved agreement with $\varepsilon_{xx,DIC}$ for both the CAD-based FEA with the Tet mesh and the CT-based FEA. The tensile strains from the CAD-based FEA with the Tet mesh performed well and matched $\varepsilon_{xx,DIC}$ at the edges of the beam (y= ±8 mm) for all load increments, while compressive strains at the edges were overestimated until the peak load increment (Fig. 6). $\varepsilon_{xx,FEA}$ from the CT-based FEA best captured $\varepsilon_{xx,DIC}$ across the face of the beam at all load increments, with near perfect agreement across all load increments.

The spatial resolution of 2D DIC measurements was limited by speckle pattern quality measures. These measures include the ratio of the individual speckle size relative to the pixel size of the captured images and the randomness of the applied speckle pattern itself. If the distribution of the speckle pattern is too sparse or too dense or if the speckles are too big the DIC software loses the ability to accurately measure small displacements. Therefore, the greater difference in $\varepsilon_{xx,DIC}$ and $\varepsilon_{xx,FEA}$ at the lower load increments is somewhat expected.

Results of the flexural moduli calculations are summarized in Table 1. Here, percent difference (PD) from the EI_{DIC} are calculated for each analysis method. The values for *EI* of the surrogate are similar to previous mechanical characterization studies of native bone as well as osteoporotic and healthy bone surrogates, 3.7-66.4, 10.3, and 22.8 x10^7 Nmm^2, respectively (Sommers et al., 2007).

Table 1: Summary of flexural rigidity results at the 6000 N load increment.

Method	*EI* (Nmm^2)	PD[a] (%)
4-pt Bending Mechanical Testing	2.60x10^7	-72
DIC	9.24x10^7	-
FEA CAD Hex	9.81x10^7	6.1
FEA CAD Tet	9.20x10^7	-0.43
FEA CT Tet	9.65x10^7	4.4
Analytical Calculation*	13.4x10^7	45

[a]PD=Percent difference from the DIC test results
*As determined by Collins et al., 2018

The largest PD in *EI* occurred between the mechanical testing and DIC results. Here, the Hertz contact deflections at an applied load of roughly 6000 N was 0.23 mm for the four-point bending mechanical testing, roughly one third of the total measured

displacement. Moreover, the mechanical test deflection data were measured from displacement of the crosshead at the upper supports. As a result, any machine compliance would result in additional overestimation of the true deflection propagating to an underestimation of the true bending stiffness of the surrogate. In contrast, the DIC data were directly measured from the surface of the surrogate, eliminating any machine compliance from the deflection data. Despite the large underestimation (-72% PD), the PD between the flexural rigidity derived from mechanical testing and DIC for the surrogate is similar to what others have found for murine femora (Arias-Moreno et al., 2020; Schriefer et al., 2005; van Lenthe et al., 2008).

Sources of deviation between EI_{DIC} and EI_{FEA} for all CAD and CT-based FEAs were limited since both were calculated using Eq. (3) and displacement measurements were taken directly from the face of the surrogate and surrogate models. As noted previously, the use of linear elastic, isotropic material properties in the FEA may misrepresent the true nature of the bone surrogate materials. However, since the mechanical testing was performed well below the yield strength of the AC or HDPU and under a quasi-static loading rate, any inelastic behaviour was unlikely to be induced during testing. Both the CAD-based and CT-based models generated with a Tet mesh outperformed the model with a Hex mesh, indicating that element type affected the accuracy of the FEA regardless of the source of the model data. The contour preserving nature of a tetrahedral mesh resulted in a better estimate of the surrogate *EI*. Interestingly, EI_{FEA} of the CAD-based model with a Tet mesh underestimated EI_{DIC}, while EI_{FEA} of the CT-based model with a Tet mesh overestimated EI_{DIC}. This difference may be due in part to the segmentation of the surrogate from the CT data, where the

clinically relevant voxel size (0.625 mm) is known to suffer from partial volume effects at the boundary. An increase in beam height (h = 25 mm) by one voxel would decrease strain by 5% in accordance with Euler-Bernoulli beam theory where strain is proportional to $1/h^2$.

The PD between EI_{DIC} and EI_x can be attributed to the EB assumption for negligible shear deflection. The dimensionless number, *S*, calculated as 0.062 for the surrogate, differentiates the static case for Timoshenko beam theory and accounts for shear deflection assumed to be negligible when using EB beam theory. This scalar can only be neglected when it is much less than one. Therefore, the span length to surrogate height ratio of roughly 2:1 resulted in an overestimation of the flexural rigidity when using EB beam theory, as is common in mammalian long bones.

The small span length to diameter ratio of the surrogate (2:1), typical of porcine long bones, did not meet the assumption of EB beam theory; and therefore, was a source of error in this method. However, the aspect ratio of murine femora, more commonly used in bone mechanical characterization studies, also do not meet this assumption (Arias-Moreno et al., 2020; van Lenthe et al., 2008). Hertz contact deflections contributed the most to deviations from EB beam theory, but shear deflection was also a contributing factor. These methodological errors are nonlinearly affected by morphology and material properties. Although acknowledged, sources of error in the DIC measurements were negligible at 6000 N.

4 CONCLUSION

The long-bone surrogate used in the current study eliminated the variance associated with analysis and testing of bone mechanical properties. The results of this study determined that CAD-based FEA was the most accurate determinant of bone surrogate *EI* and CT-based FEA was most accurate for axial strains. Analytical calculations could also be used as a relatively accurate measure of bone *EI* provided the geometry of the bone can be reasonably characterized as a prismatic beam and with the understanding that the calculated *EI* will be overestimated. Mechanical testing was the least accurate and grossly underestimated flexural rigidity of our long-bone surrogate. Simplified bone surrogates, such as the one evaluated in this study, can be designed to mimic long-bones from other large and small animal species as well as to mimic the effects of aging or disease on bone morphometry. These surrogates can then be applied to quantify errors and verify modelling and testing methods that assess bone mechanical properties.

5 ACKNOWLEDGMENTS

The authors thank Erik Polkowski, Spencer Sturton, and Max Kahn for assisting with mechanical testing of the surrogate. Funding was provided by the Hilldale Undergraduate/Faculty Research Fellowship, United States; the University of Wisconsin-Madison Graduate School, United States; and the Wisconsin Alumni Research Foundation (WARF), United States. We acknowledge the support of the Natural Sciences and Engineering Research Council of Canada (NSERC), [RGPIN/07210-2019, RGPAS/00128-2019], the Canadian Foundation for Innovation

John Evans Leaders Fund [38852], the Human Mobility Research Centre, Queen's University, Kingston, ON, Canada and the European Union's Horizon 2020 research and innovation programme under the Marie Skłodowska -Curie grant (agreement 841316). The funders had no role in study design, data collection and analysis, decision to publish, or preparation of the manuscript.

NOMENCLATURE

2D	two-dimensional
a	length of the moment arm from the upper to lower support, 12.7 mm
A	cross-sectional area of the surrogate, 938 mm^2
AC	acetyl copolymer
CAD	computer-aided design
CT	computed tomography
D	support diameter, 5 mm
DIC	digital image correlation
DICOM	Digital Imaging and Communications in Medicine
E_1	elastic modulus of the steel support (compressive), 200,000 MPa
E_2	elastic modulus of the AC shell (compressive), 2300 MPa
EB	Euler-Bernoulli beam theory
$E_{b,AC}$	experimentally measured bending modulus of the AC, 2850 MPa
EI_{DIC}	effective flexural rigidity as measured from the DIC data, Nmm
EI_{eff}	effective flexural rigidity, Nmm^2
EI_{FEA}	effective flexural rigidity from the FEAs
EI_x	analytical flexural rigidity of the surrogate about the x-axis,

	13.4×10^7 Nmm^2
F	force, N
$\bar{F}$	applied force per unit length, N/mm
F_{FEA}	force from the FEA, N
F_{max}	average maximum applied force during mechanical testing, 6026 N
FEA(s)	finite element analysis (analyses)
G	shear modulus derived from $E_{b,AC}$ and v_2, 1050 MPa
HDPU	high density polyurethane foam
HU	Hounsfield unit
h	height of the surrogate, 25 mm
K_S	bending stiffness, N/mm; $\left(\frac{F}{\delta}\right)$
L	length of the lower support span, 50.8 mm
N7/h6	locational translational fit, as described by the ASTM International Handbook, Machining
S	dimensionless number, yielding the ratio of flexural rigidity to shear rigidity and beam length
w	width, 37.5 mm
x	position at which displacements were measured, 25.4 mm
y	Hertz contact deformation at each support, mm

y_{DIC}	total localized deflection of the surrogate at the points of contact with the supports, points A and C (Fig. 1), mm
δ	displacement, mm
δ_{DIC}	measured DIC displacement, mm
δ_{FEA}	calculated displacement from the FEA, mm
$\varepsilon_{xx,DIC}$	strain in the x-direction measured using DIC
$\varepsilon_{xx,FEA}$	strain in the x-direction calculated from the FEA, measured across the face of the bone surrogate model
κ	Timoshenko shear coefficient, 0.852
v_1	Poisson's ratio of steel support, 0.3
v_2	Poisson's ratio of AC, 0.363

Figure Captions List

Fig. 1. Photo of the bone surrogate with N7/h6 fit prepped for DIC between the four-point bending supports, with coordinate system labelled.

Fig. 2 Methods used to evaluate the flexural rigidity of the bone surrogate. Here the preprocessing steps for CAD- vs CT-based finite element analysis are highlighted.

Fig. 3 Contour plot of the calculated DIC deflection (δ_{DIC}) at the peak load increment (6000N).

Fig. 4 Vertical deflection (δ) vs x-position for the 0, 1500, 3000, 4500, and 6000 N load increments, as measured by DIC (Left), CAD-based FEA with a Hex mesh (Left, Centre), CAD-based FEA with a Tet mesh (Right, Centre) and CT-based FEA with a Tet mesh (Right). δ_{DIC} data is presented as an average with 95% confidence intervals in each plot.

Fig. 5 Contour plot of the calculated DIC strain in the x-direction (ε_{xx}) at the peak load increment (6000N). Strain is reported as a percentage.

Fig. 6 Strain in the x-direction (ε_{xx}) vs y-position for the 0, 1500, 3000, 4500, and 6000 N load increments, as measured by DIC (Left), CAD-based FEA with a Hex mesh (Left, Centre), CAD-based FEA with a Tet mesh (Right, Centre) and CT-based FEA with a Tet mesh (Right). All strains are reported as a percentage and $\varepsilon_{xx,DIC}$ data is presented as an average with 95% confidence intervals in each plot.

Table Caption List

Table 1. Summary of flexural rigidity results at the 6000N load increment.

References

Arias-Moreno, A.J., Ito, K., van Rietbergen, B., 2020. Accuracy of beam theory for estimating bone tissue modulus and yield stress from 3-point bending tests on rat femora. J. Biomech. 101, 109654.

Bliuc, D., Nguyen, N.D., Milch, V.E., Nguyen, T. V, Eisman, J.A., R., C.J., 2009. Mortality risk associated with low-trauma osteoporotic fracture and subsequent fracture in men and women. J. Am. Med. Assoc. 301.

Burge, R., Dawson-Hughes, B., Solomon, D.H., Wong, J.B., King, A., Tosteson, A., 2007. Incidence and economic burden of osteoporosis-related fractures in the United States, 2005-2025. J. Bone Miner. Res. 22, 465–475. https://doi.org/10.1359/jbmr.061113

Collins, C.J., Boyer, M., Crenshaw, T.D., Ploeg, H.-L., 2018. Design of a surrogate for evaluation of methods to predict bone bending stiffness. J. Mech. Behav. Biomed. Mater. 88, 346–351. https://doi.org/https://doi.org/10.1016/j.jmbbm.2018.08.046

Dolph, C.L., 1954. On the Timoshcenko theory of transverse beam vibrations. Q. Appl. Math. 12, 175–187.

Dy, C.J., Lamont, L.E., Ton, Q. V, Lane, J.M., 2011. Sex and gender considerations in male patients with osteoporosis. Clin. Orthop. Relat. Res. 469, 1906–1912. https://doi.org/10.1007/s11999-011-1849-3

Eberl, C., 2010. Digital image correlation and tracking.

Gere, J.M., Timoshenko, S.P., 2000. Mechanics of Materials, 5th ed. USA: Brooks/Cole, Pacific Grove, CA.

Howe, C., Howe, R., Rouch, R., 1951. Application of the electronic differential analyzer to the oscillation of beams, including shear and rotary inertia, Aeronautical Research Center Eingineering Research Institute University of Michigan. UMM-67.

Iolascon, G., Moretti, A., Toro, G., Gimigliano, F., Liguori, S., Paoletta, M., 2020. Pharmacological Therapy of Osteoporosis: What's New? Clin. Interv. Aging 15, 485.

James, S.L., Abate, D., Abate, K.H., Abay, S.M., Abbafati, C., Abbasi, N., Abbastabar, H., Abd-Allah, F., Abdela, J., Abdelalim, A., 2018. Global, regional, and national incidence, prevalence, and years lived with disability for 354 diseases and injuries for 195 countries and territories, 1990–2017: a systematic analysis for the Global Burden of Disease Study 2017. Lancet 392, 1789–1858.

Jones, E.M.C., Silberstein, M.N., White, S.R., Sottos, N.R., 2014. In Situ Measurements of Strains in Composite Battery Electrodes during Electrochemical Cycling. Exp. Mech. 54, 971–985. https://doi.org/10.1007/s11340-014-9873-3

Kluess, D., Soodmand, E., Lorenz, A., Pahr, D., Schwarze, M., Cichon, R., Varady, P.A., Herrmann, S., Buchmeier, B., Schröder, C., Lehner, S., Kebbach, M., 2019. A round-robin finite element analysis of human femur mechanics between seven participating laboratories with experimental validation. Comput. Methods Biomech. Biomed. Engin. 22, 1020–1031. https://doi.org/10.1080/10255842.2019.1615481

Leslie, W.D., Morin, S.N., 2020. New Developments in Fracture Risk Assessment for Current Osteoporosis Reports. Curr. Osteoporos. Rep. 18, 115–129.

McClung, M.R., Grauer, A., Boonen, S., Bolognese, M.A., Brown, J.P., Diez-Perez, A., Langdahl, B.L., Reginster, J.-Y., Zanchetta, J.R., Wasserman, S.M., Katz, L.,

Maddox, J., Yang, Y.-C., Libanati, C., Bone, H.G., 2014. Romosozumab in Postmenopausal Women with Low Bone Mineral Density. N. Engl. J. Med. 370, 412–420. https://doi.org/10.1056/NEJMoa1305224

Morais, J.J.L., de Moura, M.F.S.F., Pereira, F.A.M., Xavier, J., Dourado, N., Dias, M.I.R., Azevedo, J.M.T., 2010. The double cantilever beam test applied to mode I fracture characterization of cortical bone tissue. J. Mech. Behav. Biomed. Mater. 3, 446–453. https://doi.org/https://doi.org/10.1016/j.jmbbm.2010.04.001

Osswald, T.A., Menges, G., 2003. Materials Science of Polymers for Engineers, 2nd ed. Hanser Gardener Publications, Inc, Cincinnati, Ohio.

Puttock, M., Thwaite, E., National Standards Labratory (Australia), 1969. Elastic Compression of Spheres and Cylinders at Point and Line Contact. Commonwealth Scientific and Industrial Research Organization, Melbourne, Australia.

Rezaei, A., Carlson, K.D., Giambini, H., Javid, S., Dragomir-Daescu, D., 2019. Optimizing Accuracy of Proximal Femur Elastic Modulus Equations. Ann. Biomed. Eng. 47, 1391–1399. https://doi.org/10.1007/s10439-019-02238-9

Ruggiero, S.L., Mehrotra, B., Rosenberg, T.J., Engroff, S.L., 2004. Osteonecrosis of the jaws associated with the use of bisphosphonates: a review of 63 cases. J. Oral Maxillofac. Surg. 62, 527–534. https://doi.org/10.1016/j.joms.2004.02.004

Schriefer, J.L., Robling, A.G., Warden, S.J., Fournier, A.J., Mason, J.J., Turner, C.H., 2005. A comparison of mechanical properties derived from multiple skeletal sites in mice. J. Biomech. 38, 467–475. https://doi.org/10.1016/j.jbiomech.2004.04.020

Sommers, M.B., Fitzpatrick, D.C., Madey, S.M., Zanderschulp, C. Vande, Bottlang, M., 2007. A surrogate long-bone model with osteoporotic material properties for biomechanical testing of fracture implants. J. Biomech. 40, 3297–3304.

van Lenthe, G.H., Voide, R., Boyd, S.K., Muller, R., 2008. Tissue modulus calculated from beam theory is biased by bone size and geometry: implications for the use of three-point bending tests to determine bone tissue modulus. Bone 43, 717–723. https://doi.org/10.1016/j.bone.2008.06.008

Wright, N.C., Looker, A.C., Saag, K.G., Curtis, J.R., Delzell, E.S., Randall, S., Dawson-Hughes, B., 2014. The Recent Prevalence of Osteoporosis and Low Bone Mass in the United States Based on Bone Mineral Density at the Femoral Neck or Lumbar Spine. J. Bone Miner. Res. 29, 2520–2526. https://doi.org/10.1002/jbmr.2269

Wysowski, D.K., Greene, P., 2013. Trends in osteoporosis treatment with oral and intravenous bisphosphonates in the United States, 2002–2012. Bone 57, 423–428. https://doi.org/https://doi.org/10.1016/j.bone.2013.09.008

Young, W.C., Budynas, R.G., Sadegh, A.M., 2002. Roark's formulas for stress and strain. McGraw-Hill New York.

Declaration of interests

☒ The authors declare that they have no known competing financial interests or personal relationships that could have appeared to influence the work reported in this paper.

☐The authors declare the following financial interests/personal relationships which may be considered as potential competing interests: